J Nanostruct 16(2): 2395-2414, Spring 2026

RESEARCH PAPER

Synthesis and Structural Characterization of a New Nano Schiff Base Ligand and its Metal Complexes: In Silico Docking, Antibacterial, and Cytotoxicity Profiling Against A549 Lung cancer

Safeer Kareem Mizher [1*], *Fawzi Yahya Wadday* [2]

[1] *Ministry of Education, The General Directorate of Educational in Najaf Al-Ashraf, Najaf, Iraq*

[2] *Department of Chemistry, Faculty of Science, Kufa University, Al-Najaf, Iraq*

ARTICLE INFO

Article History:
Received 28 November 2025
Accepted 16 March 2026
Published 01 April 2026

Keywords:
Azomethine
Cytotoxicity
Lung cancer
Metal Complexes
Nano Schiff base

ABSTRACT

A new nanoribbon, (1Z,1′Z)-N,N′-(1,2-phenylene)bis(1-(6-methoxypyridin-2-yl)methanimine) (MMAPM), was prepared by condensation of 6-methoxypicolinaldehyde with 1,2-phenylenediamine in anhydrous ethanol. Subsequently, nanocomplexes of this ribbon were formed with the metal ions cobalt(II), nickel(II), copper(II), zinc(II), platinum(IV), and gold(III). The compounds were characterized using mass spectrometry, proton nuclear magnetic resonance 1HNMR and carbon-13C NMR spectroscopy, elemental analysis (carbon, hydrogen, nitrogen, and oxygen), atomic absorption spectroscopy, ultraviolet-visible spectroscopy, Fourier transform infrared spectroscopy (FT-IR), magnetic susceptibility, molar conductivity, X-ray diffraction (XRD), and field-emission scanning electron microscopy (FE-SEM), which revealed the properties of the nanocomposites. Measured data on the structure of the metal complexes confirmed that the metal-to-bond ratio of [M(L)] for all elements except Au(III) was [M(L)2]. All the complexes exhibited non-electrolytic properties, except for the gold complex, which was conductive. The inhibitory activity against two pathogenic bacteria: Staphylococcus aureus (S. aureus) and Escherichia coli (E. coli). The study also included an in vitro evaluation of the toxicity of MMAPM and its combination with tertiary gold against human (A549) lung cancer cells and other healthy cells. Compared to the ligand, the tertiary gold complex showed a higher affinity for cancer cells while having no effect on non-cancerous cells. Molecular energy levels were calculated using density functional theory (DFT) with the B3LYP/631G base set. Using the Molecular Operating Environment (MOE) software, optimal positions for the (MMAPM) and P4+ complex were identified at receptor biosynthetic sites, suggesting this complex as a promising new drug for lung cancer cells, and its effects on other cancer types could be investigated.

How to cite this article
Mizher S., Wadday F. Synthesis and Structural Characterization of a New Nano Schiff Base Ligand and its Metal Complexes: In Silico Docking, Antibacterial, and Cytotoxicity Profiling Against A549 Lung cancer. J Nanostruct, 2026; 16(2):2395-2414.
DOI: 10.22052/JNS.2026.02.082

* *Corresponding Author Email: kareemsafeer79@gmail.com*

INTRODUCTION

Schiff bases play a pivotal role in inorganic chemistry [1] due to their ability to form stable complexes with most transition metal ions in the periodic Table. These complexes are of great importance in the medical field [2], where they are widely used in the pharmaceutical industry and exhibit high biological activity against many types of bacteria and cancer cells [3]. They are also widely used as intermediates in the synthesis of many medically and biologically important heterocyclic compounds [4]. Schiff bases can catalyze a variety of synthetic chemical processes and biologically active [5]. The emergence of inorganic biochemistry has led to increased research interest in these compounds. Metal compounds with chelating bonds to sulfur, nitrogen, and oxygen have received increasing attention due to their distinctive physical and chemical properties, especially if these compounds are heterocyclic and contain nitrogen [6,7], for their ability to act as reagents for studying DNA structure, as well as their use as chemotherapy

agents and diagnostic drugs [8]. The high electron density on the nitrogen atom in the azomethine group enhances the biological potential of these bases. Therefore, metal complexes with Schiff bases act as antioxidants, antibacterial agents, antifungals, anticancer agents, antituberculosis agents, and anti-inflammatories [9]. In this study, a diamine compound with a heterocyclic aldehyde derived from pyridine was used. Pyridine (a heterocyclic nitrogen compound) and its derivatives exhibit a wide range of biological activities [10][11] to form a Schiff base, and then the formation of complexes with cobalt(II), nickel(II), copper(II), zinc(II), platinum(III), and gold(IV). Analyses were performed to determine the structure and geometry of the compound [12]. Furthermore, the antimicrobial activity of these metal compounds was evaluated using the paper disk diffusion method [13] (for qualitative determination) and the liquid broth serial dilution method [14] (to determine the minimum inhibitory concentration). The antiproliferative activity of these compounds was investigated against various cancer cell lines [15]. Molecular docking analysis was performed to elucidate the mechanism of action of these compounds and to support the efficient binding of the molecules to the protein's active site. This study aimed to design and synthesize a novel pyridine-based Schiff base ligand and to investigate its coordination behavior with selected transition metal ions. The synthesized ligand was fully characterized using a range of physical, chemical, and spectroscopic techniques, including elemental analysis, Fourier transform infrared spectroscopy (FTIR), UV-Vis spectroscopy, mass spectrometry, and nuclear magnetic resonance spectroscopy (NMR), to confirm its structure and binding sites. A series of metal complexes with cobalt(II), nickel(II), copper(II), zinc(II), platinum(IV), and gold(III) were prepared, and their geometric structures were elucidated based on spectroscopic and magnetic studies. In addition to structural characterization, the biological potential of the ligands and their complexes was evaluated through antibacterial assays against both Gram-positive and Gram-negative bacteria, as well as in vitro anticancer studies. This work also focuses on understanding the role of metal coordination in enhancing biological activity, highlighting the synergistic effect between Schiff base ligands and metal ions.

MATERIALS AND METHODS

Instrumentation

Using the Bruker D.R.X. nuclear magnetic resonance spectrometer (NMR spectrometer). (DMSO-d6, 125 MHz, 500 MHz), a 5975 mass spectrometer, a Euro Vectro-3000A trace element analyzer, a Jena atomic absorption spectrometer (VARIO 6, AG), a Shimadzu 1700 UV-Vis spectrometer (wavelength 200-1100 nm), and a Shimadzu Fourier-transformed infrared spectrometer (wavelength 400-4000 cm^{-1}). Scanning electron microscopy (FE-SEM) images of the compounds were also acquired using a Zeiss EM3200 microscope. X-ray diffraction (XRD) was also recorded using a Philips diffraction spectrometer with a graphite crucible as the single component. The instrument used Cu kα radiation (wavelength= 1.54 angstroms) as the X-ray source at 45 kV and 50 mA. Using $AgNO_3$ solutions, the chloride content of Co(II), Ni(II), Cu(II), Zn(II), Pt(IV) and Au(III) complexes was measured. Thin-layer chromatography (TLC) was used to determine the overall composition of the materials. Selected samples were also subjected to biological activity assessments at the Al-Amin Center for Advanced Research and Biotechnology. The Beckman Model J2-21 refrigerated centrifuge and Marubeni freezer (-800°C) were manufactured in the USA. The distillation apparatus, drying apparatus,

and sterilization apparatus were manufactured by Hermle (Germany) and Ogawa Seiki (USA). Organon Teknika designed the incubators and reading devices. A Leica inverted microscope was used, and the microplates, multi-well plates, and 96-well plates—microporous membranes capable of passing through a 0.22 µm filter—were manufactured in the USA. Sterile flasks for tissue culture (25.75 cm^2), water bath, and water pump.

Materials

6-methoxypicolinaldehyde, 1,2-phenylenediamine,metal chlorides ($CoCl_2·6H_2O$), ($NiCl_2.6H_2O$, $CuCl_2.2H_2O$, $ZnCl_2$, ($H_2PtCl_6.6H_2O$) and ($HAuCl_4.3H_2O$) as well as Müller-Hinton agar, absolute ethanol, glacial acetic acid, acetone, acetonitrile, diethyl ether, dimethylsulfoxide (DMSO), hexane, N,N-Dimethylformamide (DMF), ethyl acetate. All chemicals and solvents were of the highest quality and were sourced from Sigma-Aldrich. BDH and Fluka were employed without additional manipulation.

Synthesis of New ligand (MMAPM)

The synthesis of the (1Z,1'Z)-N,N'-(1,2-phenylene)bis(1-(6-methoxypyridin-2-yl) methanimine) (MMAPM): 2.4 mL (0.02 mol) of 6-methoxypicolinaldehyde and 0.108 g (0.01 mol) of 1,2-phenylenediamine,dissolved in 20 mL of hot absolute ethanol were reacted to produce the molecule (MMAPM), with the addition of three drops of glacial acetic acid [16]. The reaction mixture was heated under reflux at 78 °C with continuous magnetic stirring to ensure complete homogeneity and successful formation. After the reaction, which lasted 270 minutes and was detected by thin-layer chromatography (TLC) using a 2:4 (v/v) mixture of hexane and ethanol as a solvent, the resulting mixture was allowed to cool gradually to room temperature and left undisturbed for 8 hours to allow crystallization and prevent agglomeration [17]. Over time, a brown crystalline substance was observed to form. The material was then washed with cold, dry ether, and the product was filtered. The solids content after oven drying was 75%. Fig. 1 illustrates the formation reaction of MMAPM.

Preparation of Metal Salts Standard Solutions

Standard solutions of metal salts were prepared by dissolving a weight of (0.0001 mol) of each of the following salts to obtain a basic solution of 1×10^{-3} M each of $CoCl_2·6H_2O$, $NiCl_2.6H_2O$, $CuCl_2.2H_2O$, $ZnCl_2$, $H_2PtCl_6.6H_2O$ and $HAuCl_4.3H_2O$ in 100 mL of absolute ethanol. These solutions were used to prepare a number of concentrations between 1×10^{-4} and 1×10^{-6} M [18].

Mole Ratio Method

The absorption spectra of 1 mL of metal ions at the optimal concentration were measured against different volumes of the bonding solution at the same concentration. A relationship was plotted between the absorption and the mole ratio, and the M:L ratio was found to be 1:1 for all the complexes under study.

Synthesis metal complexes

The Schiff base ligand (MMAPM) was coordinated with the corresponding metal chlorides of Ni(II), Co(II), Cu(II), Zn(II), Pt(IV), and Au(III) to create the metal complexes. Under constant stirring, approximately 1 mmol of the Schiff base ligand (MMAPM) was fully dissolved in 35–30 mL of hot absolute ethanol. Separately, 20–25 mL of ethanol solution was used to dissolve approximately 1 mmol of the appropriate metal chloride salt, such as $CoCl_2·6H_2O$, $NiCl_2·6H_2O$, $CuCl_2·2H_2O$,

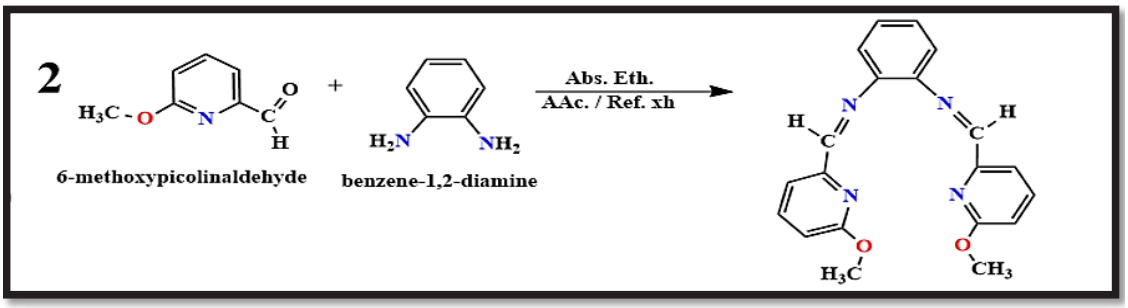

Fig. 1. Synthesis of a New Schiff Base Ligand (MMAPM).

$ZnCl_2$, $H_2PtCl_6.6H_2O$, or $HAuCl_4.3H_2O$. To guarantee full complex formation, the ligand solution was added dropwise to the metal salt solution while being continuously stirred. The mixture was then refluxed for one to three hours. The successful coordination between the ligand and metallic ions was demonstrated by the appearance of coloured precipitate [19]. The mixture was left to cool to room temperature. and the resulting solid complexes were filtered, repeatedly cleaned with cold ethanol and then diethyl ether to eliminate any materials that had not yet reacted, and oven-dried until the formation of corresponding metal (II/III/IV) Schiff base complexes, then each compound was dissolved in absolute ethanol and ultrasonically treated at a frequency of 20–40 kHz

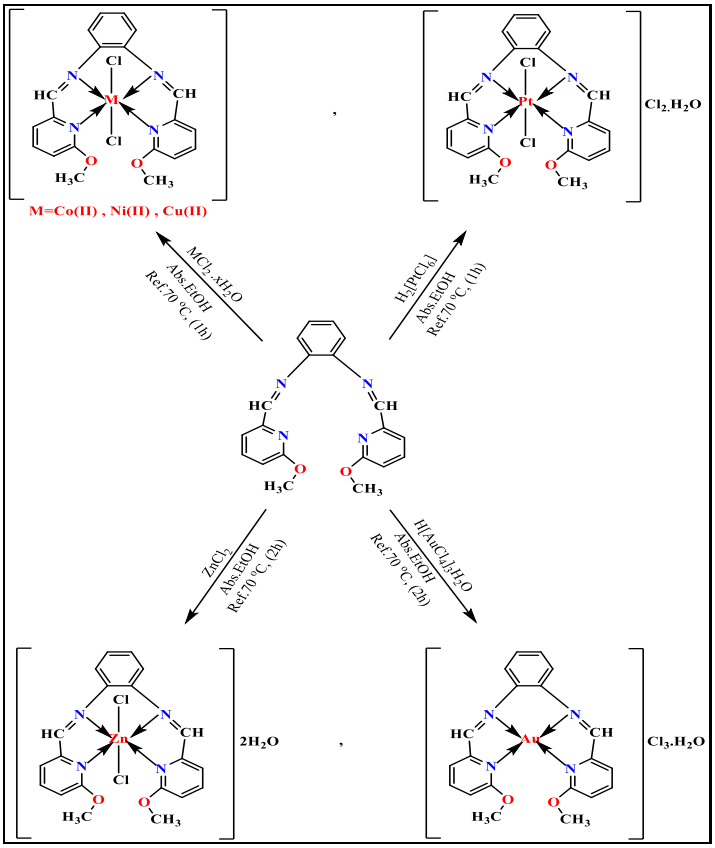

Fig. 2. Synthetic pathway for (MMAPM) complexes.

Table 1. Specific physical and chemical characteristics of the Schiff base ligand (MMAPM) and its complexes.

Compound	Color	m.p °C	λmax (nm)	Yield %	(M.wt) (g/mole)	Rf	Mole ratio [M:L]
L= (MMAPM) ($C_{20}H_{18}N_4O_2$)	Brown	155-156	443	75	346.39	0.43	---
[Co($C_{20}H_{18}N_4O_2Cl_2$)]	Red	194-196	596	81	494.24	0.44	1:1
[Ni($C_{20}H_{18}N_4O_2Cl_2$)]	Dark green	189-190	634	79	494.00	0.49	1:1
[Cu($C_{20}H_{18}N_4O_2Cl_2$)]	Green	199-201	685	83	498.85	0.49	1:1
[Pt($C_{20}H_{18}N_4O_2Cl_2$)]$Cl_2.H_2O$	Dark Page	209-211	582	71	701.29	0.41	1:1
[Zn($C_{20}H_{18}N_4O_2Cl_2$)]$2H_2O$	Reddish- brawn	179-181	439	70	518.70	0.47	1:1
Au[($C_{20}H_{18}N_4O_2$)]$Cl_3.H_2O$	Dark orange	215-217	508	66	667.72	0.50	1:1

for 20 minutes while maintaining a temperature below 40 °C to reduce agglomeration and improve nanodispersion without affecting the coordination structure. The compounds were then separated, washed, and dried [14]. The different quantities of ligand as well as the per cent composition of all forming complexes are shown below in the Table 1 and Fig. 2.

Antimicrobial Study

All recently synthesised ligands and complexes were evaluated for their antibacterial efficacy against *S. aureus* (a gram-positive bacterium) and *E. coli* (a gram-negative bacterium) utilising the agar diffusion method[20,21]. Each chemical demonstrated the ability to fight germs. The test organisms were cultivated in Mueller-Hinton broth. Chemical solutions utilised for biological study were dissolved in dimethyl sulfoxide (DMSO) at a concentration of $1x10^{-3}$ M [22]. The plates spent a day at 37°C in a heated incubator. The size of the inhibitory zone the compounds created against the corresponding test bacterium was used to assess the antibacterial efficacy of the compounds synthesised in this way. To arrive at a conclusion, the volume of the area of growth limitation for each sample was computed using the average of three independent replicates [23].

Anti-cancer studies

Using a cell viability assay against specific human cancer cell lines, the anticancer activity of the chosen compounds was evaluated in vitro [24]. The cancer cells were kept at 37°C, 5% CO_2, and humid conditions in either DMEM or RPMI-1640 with 10% FBS and 1% antibiotic-antimycotic. Trypsin-EDTA solution was used for subculturing at a confluency of roughly 70–80%. The cells were then seeded into 96-well microplates at a suitable seeding density of roughly 1×10^4 cells/well. To enable attachment, the plates were subsequently incubated for a full day. To obtain different concentrations, the chosen compounds were diluted with culture medium after being dissolved in dimethyl sulfoxide (DMSO). Fresh medium containing varying concentrations of the test compounds, untreated cells as a negative control, and a standard anticancer medication as a positive control were used to replace the culture medium after incubation. Under typical cultural conditions, the treated plates were incubated for 72 hours. Following treatment, the MTT assay—which involves adding MTT reagent to each well and then incubating for four hours was used to measure cell viability. The formed formazan crystals must be dissolved in DMSO or another suitable solubilizing solution, and a microplate reader must be used to measure the absorbance at 570 nm. In order to calculate the percentage of cell viability and inhibition, the tested compounds' IC_{50} values are derived from dose-response curves. To ensure accuracy and reproducibility, every experiment was carried out in triplicate.

Molecular Docking

The molecular docking study was conducted using the Molecular Operating Environment (MOE). The chemical structures for the ligands of interest (MMAPM, and MIMPM-Pt complex) were drawn in MOE and energy minimized with the default force field to arrive at Table three-dimensional conformations. The crystal structure of the target protein (PDB ID: 4JPS) was obtained from the Protein Data Bank, and prepared by removing water molecules and all co-crystallized ligands before adding hydrogen atoms and partial charges. The active site was obtained using the Site Finder module in MOE and docking simulations were performed with the default docking protocol, whereby ligand conformations were generated and ranked by binding free energy scores (S-score). The best binding poses were selected by choosing poses with the lowest energy according to the RMSD < 1 Å and lowest energy criteria. The interactions between the ligands and the amino acid residues at the binding site were visualized and analyzed using the MOE tools. The hydrogen bonds as well as π–π interactions and hydrophobic contacts between the ligand and the amino acid residues were easily identified, and bond distance and interaction energy could be measured.

RESULTS AND DISCUSSION

Physical features and elemental analysis

The ligand utilized in this investigation (MMAPM) is brown in colour. During the coordination process, this ligand consented with the metal ions to give complexes of varied colours. The compounds are soluble in polar organic solvents such as ethanol, methanol, acetone, diethyl ether, dimethyl sulfoxide, and carbon tetrachloride but insoluble in water. Table 2 shows the physical properties and elemental analysis (C, H, N, O) of the compound, where the analytical

data for the compounds match the experimental results. The values show a 1:1 ratio between the metal and the ligand in Co(II), Ni(II), Cu(II), Zn(II) and Pt(IV), which corresponds to an octahedral geometry. Except for the Au(III) complex, which is square planar and has the same metal-to-ligand ratio.

NMR Spectra for the (MMAPM) ligand and Pt(IV) complex

NMR spectral data were recorded for MMAPM and its complexes in DMSO-d6 solvent. The MMAPM spectrum showed a signal at 8.84 ppm attributed to the azomethine proton (-CH=N), indicating the formation of a Schiff base bond. Aromatic ring protons appeared between 7.20 and 7.57 ppm, while a signal between 7.63 and 7.67 ppm was attributed to the pyridine ring protons. A signal of 3.87 ppm was found for the methoxy group protons (-OCH_3) [25].

The non-magnetic Pt^{4+}-MMAPM complex showed a single azomethine proton (-N=CH-) signal at 8.95 ppm. Similarly, the aromatic ring protons showed a shift at (δ=7.24–7.61) ppm, and the pyridine ring protons showed a shift at (7.63–7.74) ppm. A signal at (δ=3.84) ppm was attributed to the methoxy protons directly bonded to the benzaldehyde ring in the Pt^{4+} complex, and single signals at (δ=2.31) ppm were attributed to the methyl protons directly bonded to the pyrene

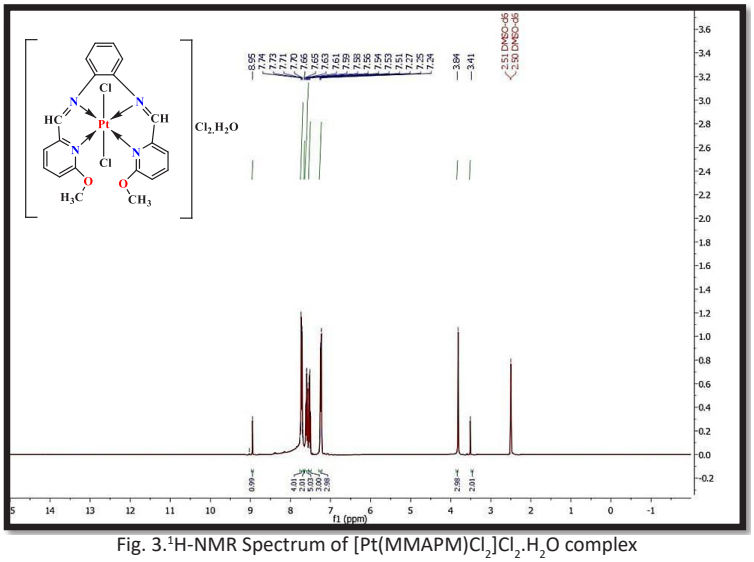

Fig. 3.^{1}H-NMR Spectrum of $[Pt(MMAPM)Cl_2]Cl_2.H_2O$ complex

Table 2. Analysis of the elemental composition of the ligand (MMAPM) and its metal complexes.

Empirical formula	M.wt g.mol^{-1}	Element analysis found (calc.) %				
		C	H	N	O	M
L = ($C_{20}H_{18}N_4O_2$)	346.39	th. 69.35 ex.(68.89)	5.24 (5.16)	16.17 (16.42)	9.24 (9.03)	-------
$[CoC_{20}H_{18}N_4O_2Cl_2]$	494.24	48.60 (48.87)	4.08 (3.94)	11.34 (11.22)	9.71 (9.89)	11.92 (11.73)
$[NiC_{20}H_{18}N_4O_2Cl_2]$	494.00	48.63 (48.21)	4.08 (4.01)	11.34 (11.49)	9.72 (9.54)	11.88 (11.97)
$[CuC_{20}H_{18}N_4O_2Cl_2]$	498.85	48.15 (47.79)	4.04 (3.95)	11.23 (11.15)	9.62 (9.83)	12.74 (12.31)
$[PtC_{20}H_{18}N_4O_2Cl_2]Cl_2.H_2O$	701.29	34.25 (33.91)	2.87 (2.90)	7.99 (8.26)	6.84 (6.97)	27.82 (26.95)
$[ZnC_{20}H_{18}N_4O_2Cl_2]2H_2O$	518.70	46.31 (46.42)	4.28 (4.31)	10.80 (11.13)	12.34 (12.17)	12.60 (12.77)
$[AuC_{20}H_{18}N_4O_2]Cl_3.H_2O$	667.72	35.98 (35.63)	3.02 (2.97)	8.39 (8.28)	7.19 (7.35)	29.50 (28.64)

ring. The peaks of the Pt-MAPM complex shifted toward the lower end of the spectrum, which is attributed to the contribution of free electron pairs in the central ion and the formation of the bond between nitrogen and Pt^{4+}[26], as shown in Fig. 3.

The ^{13}C-NMR spectra of the compound (MMAPM) in d6-dimethyl sulfoxide showed a signal at 162.03 ppm attributed to the carbon atoms in the azomethine group. The signal at 165.45 ppm was attributed to carbon atoms C16 and C19 in the pyridine ring. The shift at δ(42.53 and 42.44 ppm) was attributed to the methoxy group (CH3-O) in carbon atoms C25 and C26. The signals at (137.85), (127.64), and (123.45) ppm were attributed to the benzene diamine ring [27]. The ^{13}C-NMR spectrum of Pt^{+4} (Fig. 4) showed a slight difference in chemical shifts from the ligand spectrum. A chemical shift at δ(166.74 ppm) is attributed to the C9 atom in azomethine

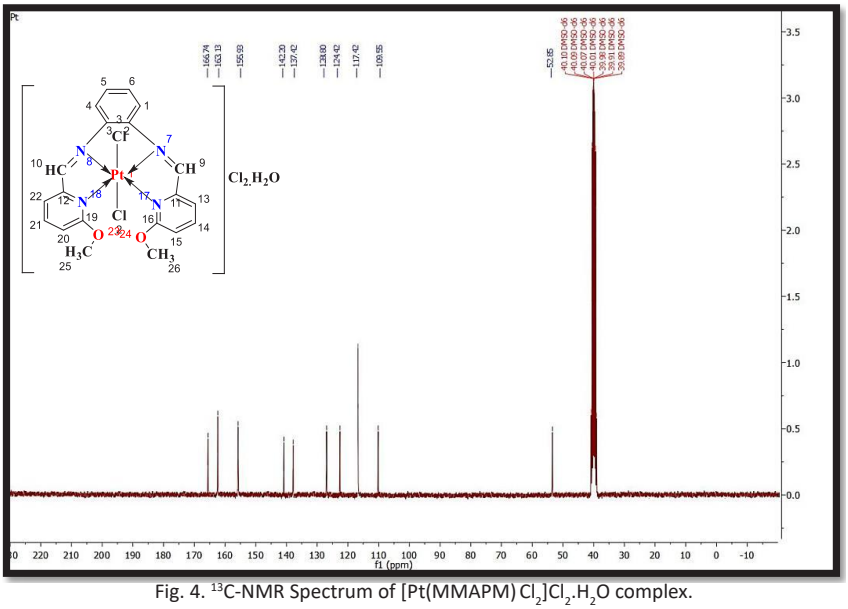

Fig. 4. ^{13}C-NMR Spectrum of [Pt(MMAPM) Cl_2]Cl_2.H_2O complex.

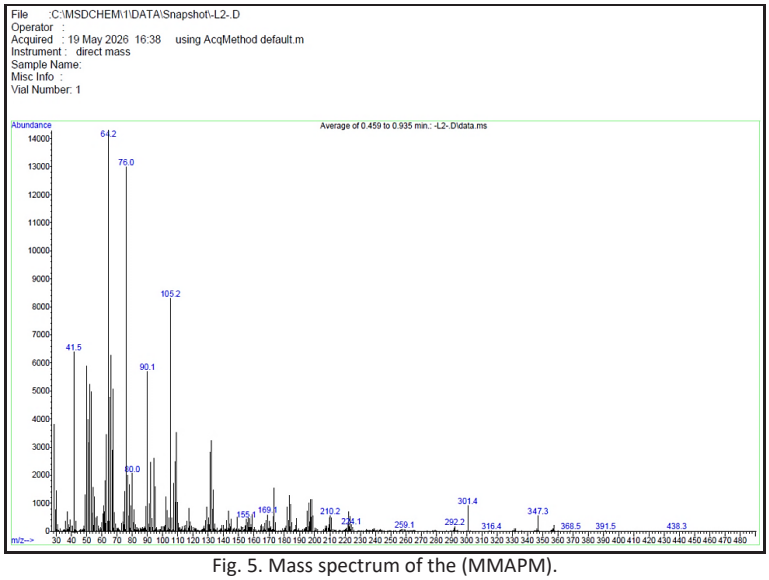

Fig. 5. Mass spectrum of the (MMAPM).

[28]. A shift at δ(166.74 ppm) is attributed to the CH_3O-C19 atoms in the pyridine rings. Chemical shifts at δ(137.42), 128.80, and 124.42 ppm are attributed to the carbon atoms of the aromatic phenyl ring [29].

The mass spectra of the ligand (MMAPM) and its Pt^{4+}-L complex were obtained in order to compare their stoichiometric composition. The base peak at (m/z^+=347) in the mass spectrum of (MMAPM) Fig. 5, a parent ion peak linked to ($M^{\cdot+}$), is believed to be a reliable indicator of the newly formed ligand. The remaining pieces, along with their respective abundances and fragmentation routes, are shown in Fig. 6. The $[PtC_{20}H_{18}N_4O_2Cl_2]Cl_2.H_2O$, similarly produced the [M^+] peaks at m/z^+ 701, which is consistent with the proposed chemical formula. The predicted chemical formula of the compounds is supported by all of these mass spectrum peak values for ligand and its investigated metal complex. Fig. 6 displays the remaining fragments, their respective abundances, and the Pt-complex's fragmentation pathways.

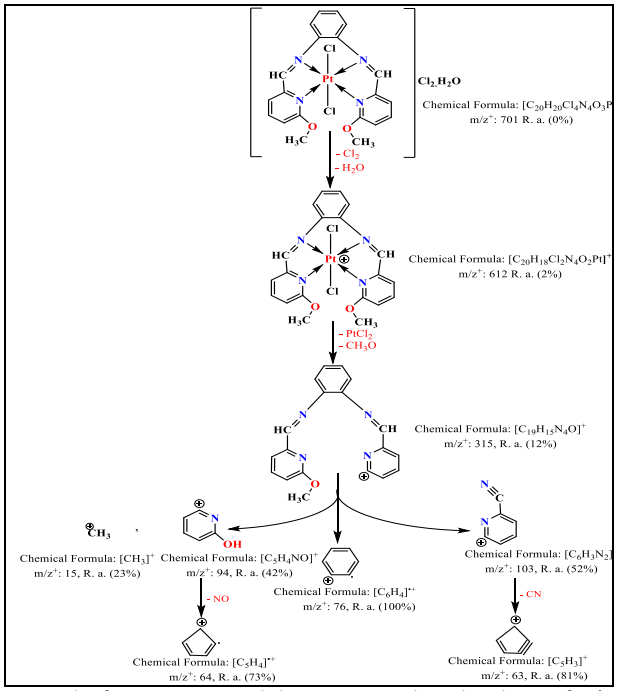

Fig. 6. The fragmentation and their corresponding abundance of Pt^{4+}-MMAPM.

Table3. IR spectra of the (MMAPM) and its complexes.

Compound	υ(H_2O) hydrate	υ(C-H) aromat.	υ(C-H) aliphat.	υ(C=N) azometh.	υ(C=N) pyr. ring	υ(C=C) aromat.	υ(C-N) pyr. ring	υM-N
L = MMAPM	-	3057	2949	1620	1590	1471	1319	-
[Co (L)Cl_2]	-	3070	2993	1600	1579	1471	1296	507-462
[Ni (L)Cl_2]	-	3072	2991	1602	1578	1469	1298	503-488
[Cu (L)Cl_2]	-	3066	2947	1600	1577	1471	1300	511-462
[Pt (L)Cl_2]$Cl_2.H_2O$	3412	3068	2985	1604	1575	1471	1305	518-482
[Zn (L)Cl_2]$2H_2O$	3389	3082	2951	1606	1581	1487	1298	509-489
[Au (L)]$Cl_3.H_2O$	3385	3072	2949	1602	1573	1473	1271	460-430

FTIR Spectra of (MMAPM) and its metal Complexes

Infrared spectral data for the Schiff base ligand (MMAPM) were collected and compared with those of its complexes for potential coordination sites in the formation of these complexes, as shown in Figs. 7 and 8. The data included in Table 3 represent the identification of characteristic bands. The ligand spectrum shows the characteristic -C=N band at 1590 cm^{-1}, and this band shifts to lower frequencies in the spectra of the complexes and is observed at 1579, 1578, 1577, 1575, 1581, and 1581 cm^{-1} in the spectra of the complexes with Co^{+2}, Ni^{+2}, Cu^{+2}, Zn^{+2}, Pt^{+4} and Au^{+3}, respectively [30]. This indicates the participation of azomethine nitrogen in the formation of the bond with the metal ions [31]. The binding of nitrogen to metal ions reduces the electron density on the azomethine bond, leading to a decrease in the absorption of –C=N-. The bands at 3412 cm^{-1} for the platinum complex, 3389 cm^{-1} for the zinc complex, and 3385 cm^{-1} for the gold complex indicate the presence of water of crystallization molecules [32]. Furthermore, the infrared spectra of these complexes reveal new bands in the 507, 503, 511, 518, 509, and 526 cm^{-1} regions, which suggest (M-N) binding, respectively [33]. The appearance of (M-N) supports the involvement of a nitrogen atom in the formation of these complexes under study.

Electronic spectra and magnetic measurements

The UV-Vis spectrum of the methyl phosphate group (MMAPM) in Table 4 shows a high-intensity absorption peak at 223, 240, and 291 nm, attributed to (π→π*) transitions. A band at 443 nm is also present, attributed to n→π* transitions of the azomethine nitrogen electron pair to the Schiff base [34]. As these bands shift to higher

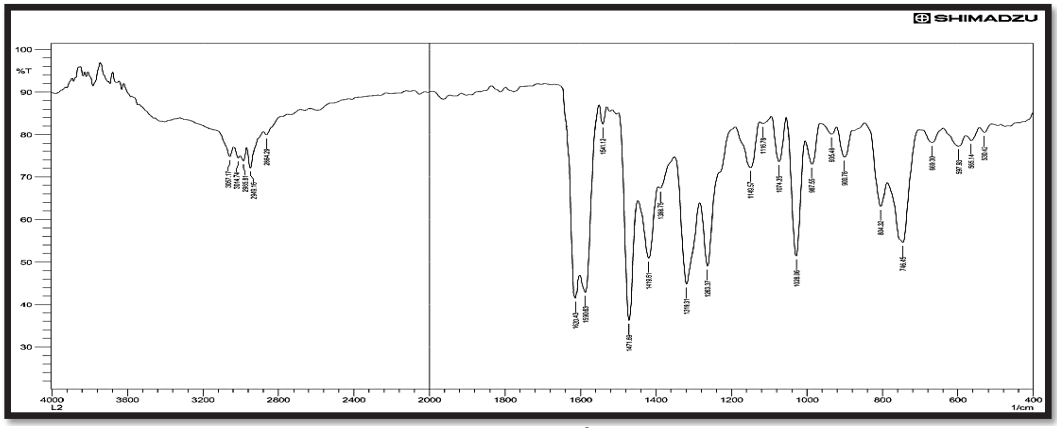

Fig. 7. FT-IR spectrum of MMAPM.

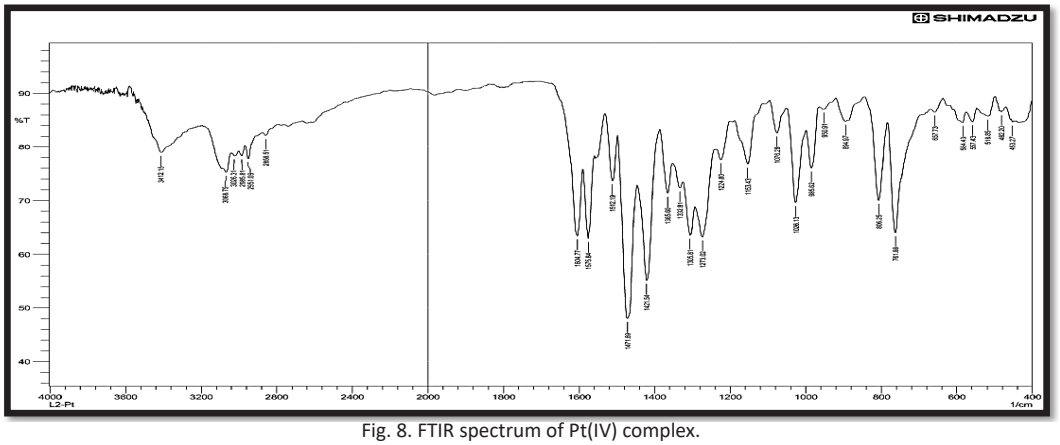

Fig. 8. FTIR spectrum of Pt(IV) complex.

wavelengths, the azomethine nitrogen binds to the central metal ion during the formation process. Physical evidence for all these observations is found in the red color of the Cobalt ion's complex. Both bands appearing in Fig. 9 at 596 nm and 672 nm are caused by the $^4T_1g(F) \rightarrow {}^4T_1g(p)$ (υ_3) and

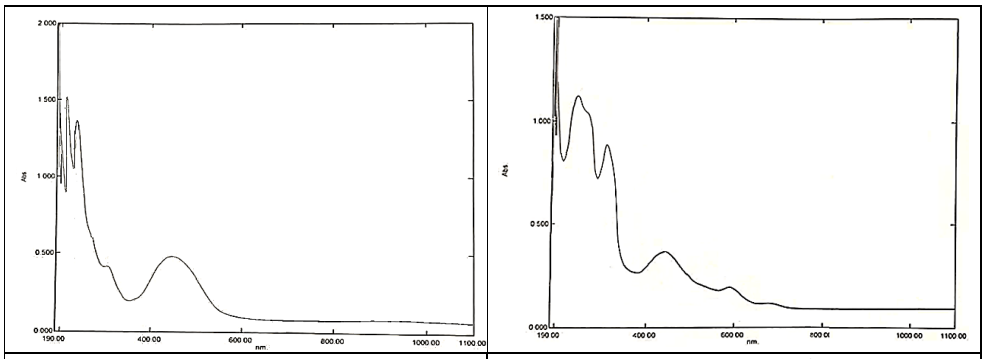

MMAPM | [Co (MMAPM)Cl_2]

Fig. 9. Electronic spectrum of Co (II) complex with MMAPM.

Table 4. Electronic spectra, magnetic measurements, geometries and hybridization of metal complexes of (MMAPM) under study at laboratory temperature.

Compounds	λ_{max} (nm)	Absorption Bands (cm^{-1})	Transitions	μ_{eff} (B.M)	Geometry	Hybridization
L = (MMAPM)	443	22573.36	n →π*	-	-	-
	291	34364.26				
	240	41666.66	π →π*			
	223	44843.04				
Co(II)-Complex	672	14880.95	$^4T_1g \rightarrow {}^4A_2g_{(F)}(\upsilon_2)$	4.266	Octahedral (Distorted)	sp^3d^2 High spin
	596	16778.52	$^4T_1g \rightarrow {}^4T_1g_{(p)}(\upsilon_3)$			
	431	23201.85	n →π*			
	304	32894.73	π →π*			
	270	37037.03	π →π*			
	252	39682.53	π →π*			
Ni(II)-Complex	749	13351.13	$^3A_2g \rightarrow {}^3T_2g_{(F)}(\upsilon_1)$	2.950	Octahedral	Sp^3d^2 High spin
	634	15772.87	$^3A_2g \rightarrow {}^3T_1g_{(F)}(\upsilon_2)$			
	423	23640.66	n →π*			
	341	29325.51	π →π*			
	282	35460.99	π →π*			
	218	45871.55	π →π*			
Cu(II)-Complex	685	14598.54	$^2B_1g \rightarrow {}^2A_1g$ (dx2-y2→dz2) (υ_1) $^2B_1g \rightarrow {}^2B_2g$ (dx2-y2→dyz) (υ2) $^2B_1g \rightarrow {}^2B_2g$ (charge transfer) (υ3)	1.852	Octahedral (Distorted)	Sp^3d^2 High spin
Zn(II)-Complex	431	23201.85	n →π*	Dia	Octahedral	Sp^3d^2 Low spin
	393	25445.29	π →π*			
	266	37593.98	π →π*			
	219	45662.10	π →π*			
	439	22779.04	$d\pi(Zn)^{+2} \rightarrow \pi^*(L)$(C.T)			
	410	24390.24	n →π*			
	280	35714.28	π →π*			
	229	43668.12	π →π*			
Pt(IV)-Complex	698	14326.64	$^1A_1g \rightarrow {}^1T_2g_{(F)}(\upsilon_2)$	Dia	Octahedral	d^2Sp^3
	582	17182.13	$^1A_1g \rightarrow {}^1T_1g_{(p)}(\upsilon_3)$			
	405	24691.35	n →π*			
	306	32679.73	π →π*			
	279	35842.29	π →π*			
	250	40000.00	π →π*			
	228	43859.64	π →π*			
Au(III)-Complex	794	12594.45	$^1A_1g \rightarrow {}^1T_1g_{(F)}(\upsilon_1)$	Dia	Square Planer	dsp^2 Low spin
	681	14684.28	$^1A_1g \rightarrow {}^1B_1g(\upsilon_2)$			
	508	14684.28	$^1A_1g \rightarrow {}^1Eg(\upsilon_3)$			
	402	24875.62	n →π*			
	326	30674.84	π →π*			
	254	39370.07	π →π*			
	223	44843.04	π →π*			

$^4T_1g(F)\rightarrow{}^4A_2g(F)$ (υ_2) transitions, respectively, with octahedral structures. The Nickel(II) complex has a magnetic moment of 2.950 B.M. These results can be attributed to two visible bands at 749 nm and 634 nm, which indicate the presence of the $^3A_2g\rightarrow{}^3T_2g(F)(\upsilon_1)$ and $^3A_2g\rightarrow{}^3T_1g(F)$ (υ_2) electron transitions associated with the octahedral nickel(II) complex [35]. The broad absorption band of Cupper(II) at 685 nm has been attributed to the $^2B_1g\rightarrow{}^2A_1g$, $^2B_1g\rightarrow{}^2B_2g$, and $^2B_1g\rightarrow{}^2B_2g$ transitions, with a magnetic moment value of 1.852 B.M, consistent with distorted octahedral structures. The blue-shifted bands in the Zn(II) complex's spectrum 439 nm indicate that the azomethine group coordinates or is assigned to the dπ(Zn) $^{2+}\rightarrow$ π*(L)(C.T) transition. Electronic spectrum data for the Zn(II) complex shows a octahedral, diamagnetic configuration[26]. Electron spectral data for Platinum(IV) in ethanol were also collected, and when compared to the spectrum of the free ligand, bands at 698 and 582 nm were associated with the $^1A_1g\rightarrow{}^1T_2g(F)$ (υ_2) and $^1A_1g\rightarrow{}^1T_1g(p)$ (υ_3) transitions, while the bands at 405 nm confirm the (n→π*) transition. This also confirms the regular octahedral geometry of platinum(IV) [36]. The electronic spectrum of Au(III) complexes shows a band at 794 nm for the $^1A_1g\rightarrow{}^1T_1g(F)$ (υ_1) transition and a band at 681 nm for the $^1A_1g\rightarrow{}^1B_1g(\upsilon2)$ transition. A band at 508 nm indicates the $^1A1g\rightarrow{}^1Eg$ (υ3) transition, while bands at 402–223 nm indicate intrabond transitions (n→π*). The study shows that the Au(III) complex is non-magnetic and has a planar square shape [37]. With a blue shift in the ligand spectrum (MMAPM) and the appearance of new bands, these complexes exhibit bright colors, indicating symmetry between the ligand and the metal ion. Table 4 shows the basic electronic transitions of the MMAPM ligand and metal complexes.

Conductivity measurements

The molar conductivity of the studied metal complexes was investigated using absolute ethanol as a solvent at room temperature, as shown in Table 5. The conductivity ratio of the metal complexes with the MMAPM ligand was found to be 0:0, while it was 1:2 with platinum (IV), and 1:3 with gold (III). The values for the other compounds were found to be similar to those obtained for many non-ionic metal compounds [38].

X-ray diffraction study (XRD)

Using X-ray diffraction in the solid state, the ligand (MMAPM) as well as their metal complexes under investigation were examined in the angular range of 2 (5-80°) to ascertain certain structural characteristics, including crystal sizes and structure. To ascertain their purity and the flaws in the crystal structure that arose when the ligands under investigation were transformed into metal complexes, microstrains and dislocation density were also computed. Certain diffraction peaks arise for the reasons listed in : First, microstrain (like lattice deformation); second, faulting due to crystal distortions; Third: The crystal's domain size; fourth: The domain size distribution [28]. The distance (d spacing) between the crystal planes for the ligand as well as their metal complexes was determined using Bragg's law [39]. For the ligands and their prepared metal complexes, the X-ray diffraction (XRD) spectra showed a distinct difference in the previously mentioned data of the density of solutes (δ), micro-ductility (Ψ), crystal size (D), and the spacing between the crystal planes (d). We observed an inverse relationship between the crystal size (D), micro-ductility (Ψ), and the density of solutes (δ); as the crystal size increases, the micro-ductility decreases, the density of solutes decreases, and consequently

Table 5. Molar conductivity values (mΛ) for ligand MMAPM in solid metal complex solutions in absolute ethanol at ambient temperature and at a concentration of (1×10^{-3}).

Metal Complexes	Molar conductivity $S.cm^2.mol^{-1}$	Electrolyte nature
$[Co(MMAPM)Cl_2]$	12.36	Non
$[Ni(MMAPM)Cl_2]$	13.31	Non
$[Cu(MMAPM)Cl_2]$	12.44	Non
$[Zn(MMAPM)Cl_2]2H_2O$	13.68	Non
$[Pt(MMAPM)Cl_2]Cl_2.H_2O$	78.33	Ionic
$[Au(MMAPM)]Cl_3.H_2O$	115.9	Ionic

the defects in the crystal decrease. This confirms the occurrence of the coordination process between the ligands and the metal ions under study. Because of micro-tension and crystalline cracking, the lack of sharp peaks suggests the absence of a crystalline network. In X-ray spectroscopy, amorphous structures are indicated by broad peaks, whereas crystalline or semi-crystalline structures are indicated by sharp peaks. The crystalline arrangement, the characteristics of the crystalline network, and the crystalline planes all affect how sharp these peaks are. Furthermore, it was demonstrated to us that all of the ligand and their metal complexes under investigation are in the nano range because their grain sizes are less than 100 nm. The diffraction angles, observed d values, relative intensity, crystal size, crystal intensity, peak widths at mid-intensity, micro-resistance, and dissolution density for each ligand. Displayed in the X-ray spectrum in Table 6 and the metal complexes that are being investigated. The X-ray diffraction spectra of the ligand and their prepared metal complexes are shown in Fig. 10.

FE-SEM analysis

The ligand (MMAPM) and its metal complexes' surface characteristics, including particle size, shape, aggregates, and distribution, were examined Fig. 11. The irregular fragments particles with an average particle size of 36.41 nm were visible in the FESEM image of the ligand. The Zn(II) complex FESEM image revealed clumped with an average particle size of 40.83 nm and the largest percentage of clusters. The Au(III) complex's FESEM image revealed heterogeneous crystals with a lower proportion of aggregates particles with an average particle size of 45.62 nm, whereas the Pt(IV) complex's FESEM image revealed

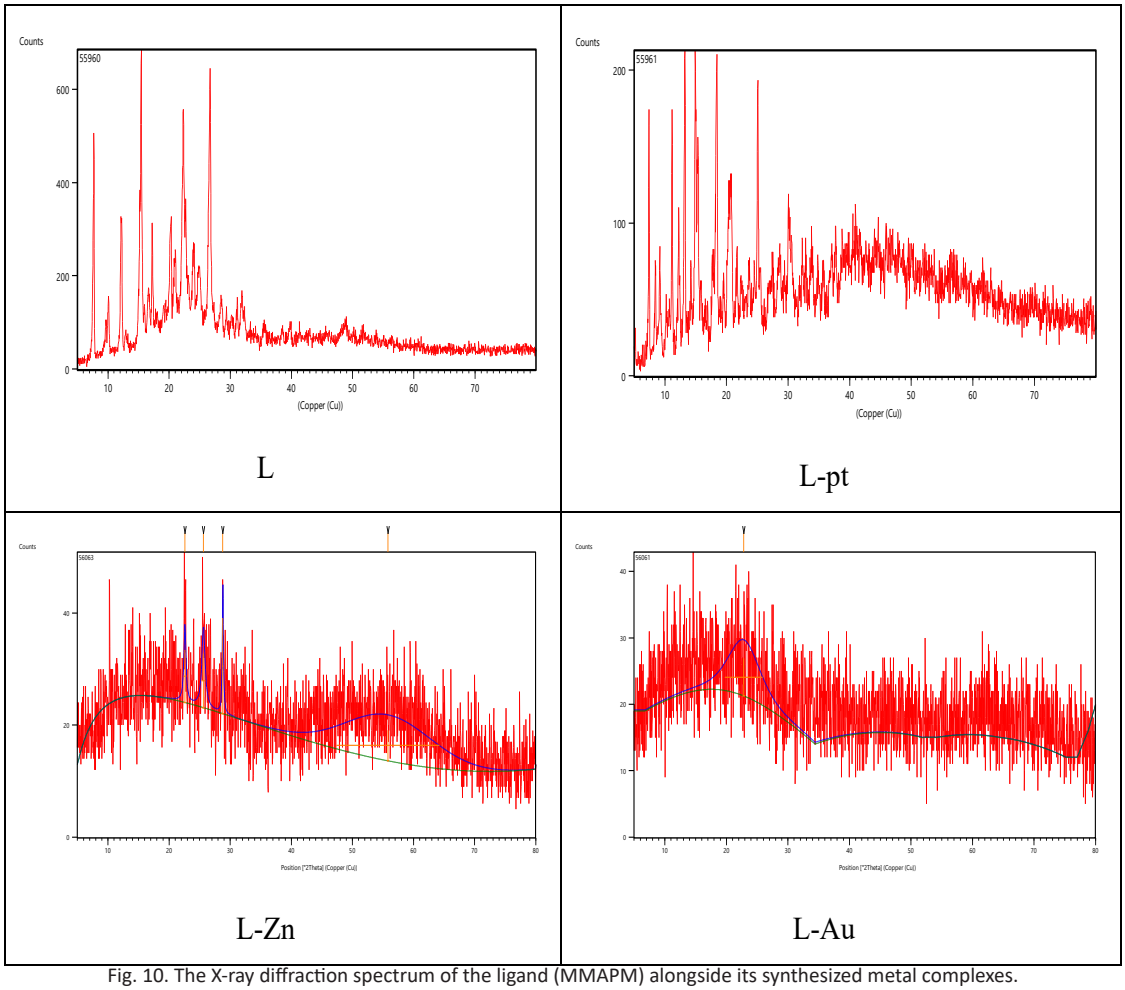

Fig. 10. The X-ray diffraction spectrum of the ligand (MMAPM) alongside its synthesized metal complexes.

irregular with an average particle size of 380.07 nm [40].

Suggested configurations for prepared compounds

All complexes are octahedral in geometry, with the exception of the gold, palladium, and silver complexes, which are square planar and tetrahedral, respectively, according to the literature on the available coordination sites in the ligand and its relationship with different metal ions [41].These findings were obtained using spectroscopic and analytical methods such as molar ratio diagnostic measurements, elemental analysis, metal content, magnetic measurements, molar conductivity, and UV-visible and Fourier transform infrared spectroscopy. The coordination was established through the nitrogen atoms of the azomethine groups, resulting in five-membered chelate rings that add stability to the formed metal complexes. In all complexes, the ligand uses a bidentate coordination mechanism [42]. The interactions mentioned above are shown in Fig. 12, which was created with Chem. Sketch 2020. These structures exhibit metal to ligand ratios of 1:2 and 1:1, as predicted by our approach.

Antibacterial activity

Pyridine and its derivatives exhibit significant activity in inhibiting numerous pathogenic bacteria and fungi [43]. This is attributed to the ability of its solutions to dissolve the outer cell wall, leading to leakage of cell fluids and cell death. Furthermore, this biologically active ligand contains functional groups within its structure, such as two hybridized nitrogen atoms, enabling it to bind to various elements present in the cell body [44], such as copper, cobalt, iron, zinc, divalent manganese, and monovalent potassium ions, which are essential for bacterial cell function. This results in the formation of complexes with these elements, which in turn

Table 6. lists the diffraction angles, observed d values, relative intensity, average size, peak widths at mid-intensity, and crystal dimensions for each ligand (MMAPM) and some its complexes.

Compound	Pos. [°2Th.]	Height [cts]	FWHM [°2Th.]	d-spacing [Å]	Rel. Int. [%]	Tip width [°2Th.]	Crystallite Size D (nm)	Dislocation density δ $\times10^{-3}$ (nm^{-2})	Microstrain ε $\times10^{-3}$	Average size (nm)
MMAPM	14.8628	903.67	0.3444	5.96061	49.69	0.4133	24.286081	1.695451	11.520	24.63
	19.1844	1818.67	0.2952	4.62653	100.00	0.3542	28.494285	1.231642	7.620	
	21.1860	924.26	0.2460	4.19372	50.82	0.2952	34.299706	0.850001	5.740	
	23.9731	1664.99	0.2952	3.71210	91.55	0.3542	28.722332	1.212162	6.070	
	26.2830	689.84	0.3936	3.39087	37.93	0.4723	21.638826	2.135662	6.650	
	28.9708	503.01	0.3936	3.08211	27.66	0.4723	21.764088	2.111115	6.650	
	36.7015	178.42	0.3936	2.44872	9.81	0.4723	22.206104	2.028763	5.180	
	47.2658	1286.57	0.5904	1.92314	70.74	0.7085	15.334907	4.252435	5.890	
Au(III)-Complex	14.4367	950.73	0.3401	5.90711	50.31	0.4112	25.944276	1.481087	10.517	26.52
	19.2874	1800.31	0.2942	4.62364	100.00	0.3573	29.897324	1.115663	8.223	
	24.1231	920.37	0.2547	4.19052	51.83	0.3099	35.112053	0.828331	6.792	
	29.8447	1650.43	0.2922	3.71317	92.36	0.3542	28.017723	1.282187	7.574	
	39.6448	690.75	0.3982	3.39226	38.25	0.4710	21.932351	2.060925	5.928	
	50.0277	500.42	0.3911	3.08933	28.28	0.4785	18.233174	3.092284	5.250	
Zn (II)-Complex	14.8978	900.17	0.3423	5.90123	45.42	0.4112	26.335156	1.372156	10.032	27.43
	19.6984	1700.64	0.2976	4.62321	100.00	0.3554	31.011231	1.041783	8.163	
	24.5647	2300.23	0.2521	3.52124	85.25	0.3077	35.833627	0.770932	6.605	
	29.4226	1500.66	0.2918	3.71095	65.73	0.3536	29.201124	1.195345	7.312	
	38.2394	680.52	0.3955	3.39435	32.56	0.4717	23.351234	1.891153	5.810	
	48.9774	480.65	0.3928	3.08125	28.23	0.4722	18.854832	2.776245	5.154	
Pt(IV)-Complex	15.3112	950.22	0.3409	5.90217	40.85	0.4183	25.341213	1.603179	10.289	25.74
	20.1103	1800.15	0.2966	4.62095	100.00	0.3542	29.521351	1.192316	8.062	
	25.1102	2360.55	0.2524	3.52325	85.33	0.3021	34.536420	0.861021	6.823	
	29.9884	1600.43	0.2910	3.71834	68.65	0.3517	28.122145	1.289334	7.452	
	40.2013	700.65	0.3938	3.39234	30.25	0.4793	21.238794	2.060452	5.904	
	48.6673	500.44	0.3916	3.00381	21.92	0.4725	17.175936	3.099212	5.390	
	15.6324	950.45	0.3441	5.90612	40.85	0.4119	24.256376	1.606211	10.245	

cause cell death due to the loss of these elements [45]. The biological activity of the ligand and its metallic compounds under investigation was studied against two different types of pathogenic bacteria, one Gram-positive (*S. aureus*) and the other Gram-negative (*E. coli*). Platinum (IV), zinc (I), and gold (III) complexes demonstrated high activity against both Gram-positive and Gram-negative bacteria. The biological activity results showed high inhibitory activity against both types

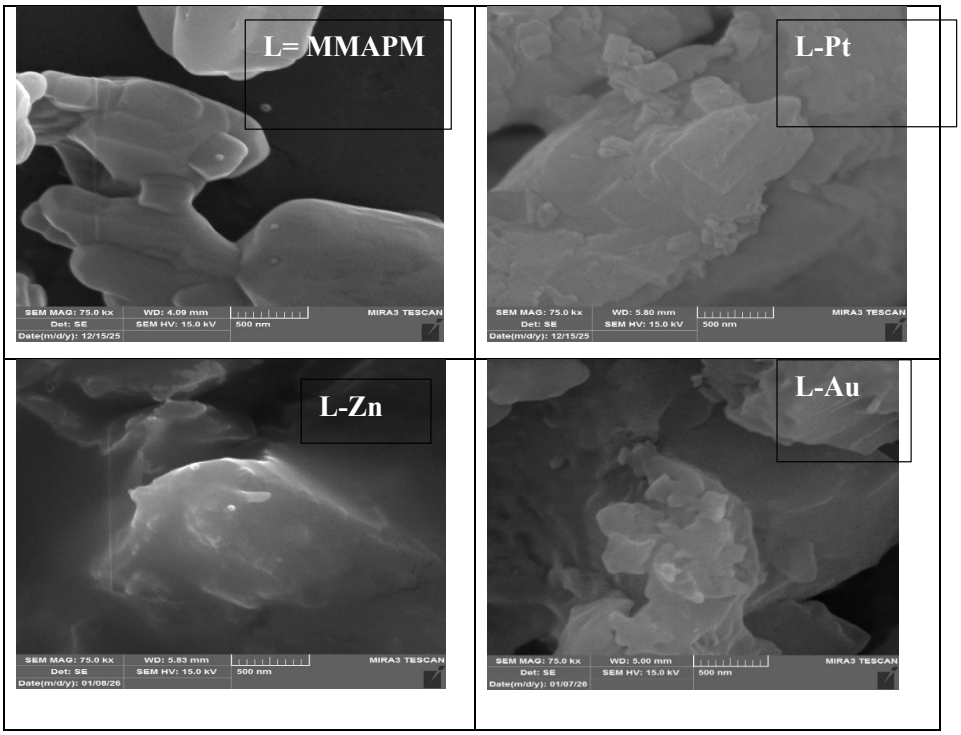

Fig. 11. FE-SEM images of ligand (MMAPM) and its prepared complexes.

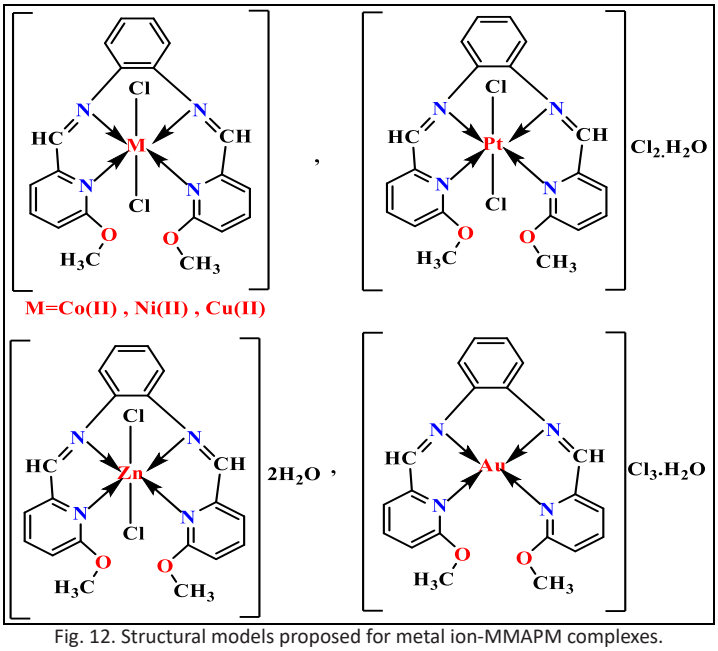

Fig. 12. Structural models proposed for metal ion-MMAPM complexes.

of bacteria used. Inhibition zones (in millimeters) were recorded to study the effects of the ligand and its prepared metal compounds dissolved in 0.1 mg/ml dimethyl sulfoxide (DMSO) on Staphylococcus aureus and Escherichia coli. Table 7 and Fig. 13 show the results.

Molecular docking

The theoretical study used the (MOE) Molecular Operating Environment program to show the molecular docking mechanism of the ligand (MMAPM) Schiff base and its complexes $[PtLCl_2]$ $Cl_2.H_2O$ with lung cancer protein (4JPS). Following molecular docking with the (4JPS) protein, the two compounds showed strong binding affinities with varying degrees of stability in the active pocket. The strongest binding -5.0084 kcal/mol, was achieved with the standard ligand,

Table 7. Shows the effects on the two types of bacteria of ligand (MMAPM) as well as their metal complexes dissolved in DMSO at a concentration of 0.1 mg/mL.

Compound	Bacteria	
	Gram-Positive	Gram-Negative
	S. aureus	*E.coli*
DMSO	0	0
(MMAPM) = ($C_{20}H_{18}N_4O_2$)	19	20
[Co $C_{20}H_{18}N_4O_2Cl_2$]	21	21
[Ni $C_{20}H_{18}N_4O_2Cl_2$]	20	21
[Cu $C_{20}H_{18}N_4O_2Cl_2$]	24	22
$[PtC_{20}H_{18}N_4O_2Cl_2]Cl_2.H_2O$	20	19
$[ZnC_{20}H_{18}N_4O_2Cl_2]2H_2O$	21	19
$[AuC_{20}H_{18}N_4O_2]Cl_3.H_2O$	19	18

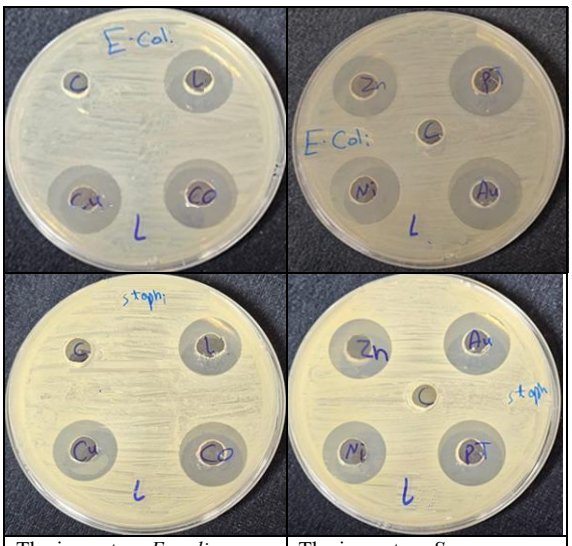

The impact on *E. coli* of the ligand, and its metal complexes | The impact on *S. aureus* of the ligand and its metal complexes

Fig. 13. The effect of (MMAPM) and its metal complexes on *E.coli* and *S. aureus* as well as DMSO solvent at a concentration of 0.1 mg/mL.

indicating a stable and well-fitted complex inside the receptor cavity. The other two compounds had less negative values, indicating weaker but still favorable binding interactions.

Docking results for ligand (MMAPM)

Compound (MMAPM) (pose 1) achieved a moderate affinity (-6.90783 kcal/mol) but had the lowest RMSD (1.795422 Å), indicating a highly stable conformation even if the total binding energy was slightly weaker. This suggests a precise geometric fit that could be optimized further to strengthen polar interactions. Moreover it can make hydrogen bond with TYR 836, TRP 780, TRP 780, GLN 859 as displayed in Table 8.

Molecular docking of the compound $[PtC_{20}H_{18}N_4O_2Cl_2]Cl_2.H_2O$

The complex $[Pt(MMAPM)Cl_2]Cl_2.H_2O$ exhibited the best docking performance, with a binding affinity of -5.0084 kcal/mol and an excellent RMSD value of 1.643115 Å angstrom, reflecting high stability within the binding pocket. Its interactions included strong hydrogen bonds with the amino acid residues VAL 851 and MET 922, which enhances its stability [46]. The polar and nonpolar

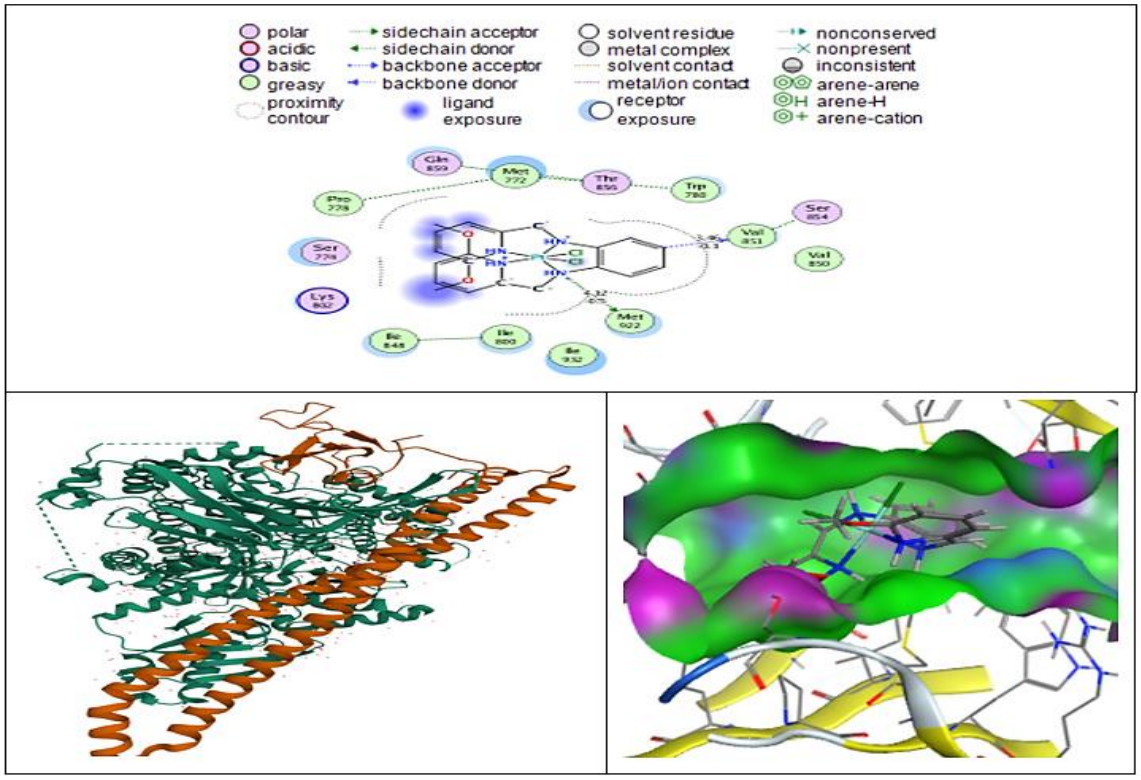

Fig. 14. 2D and 3D images, along with a detailed analysis of the interaction between the $[Pt(MMAPM)Cl_2]Cl_2.H_2O$ and the protein (4JPS).

Table 8. Details of the best poses of ligand (MMAPM) with protein (4JPS).

Compounds	Binding Affinity Kcal/mol	Rmsd (Å)	Atom of compound	Atom of Receptor	Involved receptor residues	Type of interaction bond	Distance (Å)	E (kcal/mol)
MMAPM	-6.90783	1.795422	C 21	6-ring	TYR 836	(A) H-pi	3.6	-0.6
			C 26	6-ring	TRP 780	(A) H-pi	5.04	-0.3
			6-ring	NH2	ARG 770	(A) pi-cation	4.4	-1.2
			6-ring	CZ3	TRP 780	(A) pi-H	4.35	-0.2
			6-ring	NE2	GLN 859	(A) pi-H	3.74	-1.5

interactions make compound the most promising candidate, as it approaches the standard drug-binding efficiency. This good binding pattern with the protein (4JPS) supports its strong inhibitory activity, with an IC50 value of 150 µg/ml [47]. Table 9 and Fig. 14 below illustrate this interaction.

Effect of the ligand (HDF)

The ligand (MMAPM) and its combination with $[Pt(MMAPM)Cl_2]Cl_2.H_2O$ were tested for their anticancer activity against A549 lung cancer cells. Novel bioactive compounds with selective cytotoxicity are important for cancer treatment. Cell viability and the anticancer activity of these compounds were measured using the MTT assay [48]. The results showed that (MMAPM) possesses high inhibitory energy against cancer cells. The inhibition was highest at the highest concentration (400 µg/ml). The inhibition percentage of the ligand and its combination with platinum was 61.04% and 71.38%, respectively, at this dose. At the lowest concentration (25µg/ml), the A549 cell line showed only slight inhibition, at percentages of 25.17% and 24.12%, respectively. The IC_{50}

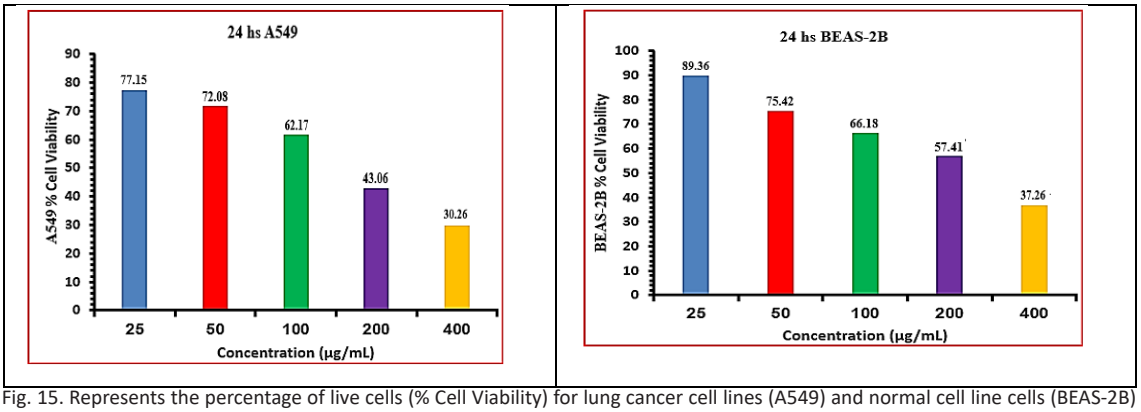

Fig. 15. Represents the percentage of live cells (% Cell Viability) for lung cancer cell lines (A549) and normal cell line cells (BEAS-2B) versus the concentration of the complex $[Pt(MMAPM)Cl_2]Cl_2.H_2O$.

Table 9. Details of the best poses of $[Pt(MMAPM)Cl_2]Cl_2.H_2O$ with protein (4JPS).

	Binding Affinity Kcal/mol	Rmsd (Å)	Atom of compound	Atom of Receptor	Involved receptor residues	Type of interaction bond	Distance (Å)	E (kcal/mol)
$[Pt(MMAPM)Cl_2]Cl_2.H_2O$	-5.0084	1.643115	C 9 N 12	O SD	VAL 851 MET 922	(A) H-donor (A) H-donor	3.46 4.12	-0.3 -0.5

Tables 10. Show the effect of the ligand (MMAPM) on the growth of lung cancer cell lines (A549) and comparing it with the normal cell line (BEAS-2B) for the same concentration using the MTT test for a period of 24 hours.

Con. ($\mu g.mL^{-1}$)	Mean Percentage (%) for each cell line					
	A549			BEAS-2B		
	Cancerous line cells of A549			Normal line cells of BEAS-2B		
	Cell Viability	SD	Cell Inhibition	Cell Viability	SD	Cell Inhibition
25	76.48	2.271	25.17	90.02	2.215	11.84
50	72.36	3.943	29.52	76.23	2.341	25.63
100	61.84	1.362	40.27	67.04	0.472	34.62
200	43.17	1.371	58.34	57.24	3.133	44.18
400	30.61	4.911	61.04	37.38	1.525	64.21
	IC50= 150			IC50=105.35		

Table 11. Show the effect of the platinum (IV) complex on the growth of lung cancer cell lines (A549) and comparing it with the normal cell line (BEAS-2B) for the same concentration using the MTT test for a period of 24 hours.

Con. ($\mu g.mL^{-1}$)	Mean Percentage (%) for each cell line					
	A549			(BEAS-2B)		
	Cancerous line cells of A549			Normal line cells of (BEAS-2B)		
	Cell Viability	SD	Cell Inhibition	Cell Viability	SD	Cell Inhibition
25	77.15	1.815	24.12	89.36	2.453	12.32
50	72.08	3.271	29.63	75.42	2.226	26.34
100	62.17	3.364	39.45	66.18	1.647	35.26
200	43.06	4.116	58.74	57.41	2.638	44.52
400	30.26	4.714	71.38	37.26	1.529	64.35
	IC50=185			IC50= 84.45		

values also confirmed the selective toxicity of A549 lung cancer cells at 150 µg/ml for (MMAPM) and 197 µg/ml for platinum. For normal (BEAS-2B) cells, the IC_{50} values were 220 µg/ml.These results indicate that platinum(IV) selectively damages lung cancer cells without affecting normal cells, supporting its potential as a novel anticancer therapy. Table 10 and Fig. 15 illustrate the dose-dependent effects on A549 prostate cancer cells compared to normal (BEAS-2B) cells using the 24-hour MTT assay at 37°C.

CONCLUSION

The complexes in this study were characterized using proton (^{1}H) and (^{13}C) nuclear magnetic resonance, elemental analysis, mineral composition analysis, Fourier transform infrared (FT-IR) and ultraviolet-visible (UV-Vis) mass spectrometry, X-ray diffraction (XRD), and field emission scanning electron microscopy (FE-SEM). Magnetic susceptibility measurements indicated that the octahedral configuration was correct for all complexes except for the gold(III) complex, which exhibited a planar square geometry. The M:L ratio in these structures was 1:1. The bioactivity data for the compounds showed antibacterial and anti-lung cancer properties.

CONFLICT OF INTEREST

The authors declare that there is no conflict of interests regarding the publication of this manuscript.

REFERENCES

1. Yadav S, Yadav D, Verma P, Kumar V. Synthesis, Spectroscopic Characterization, Thermal Behavior, and Antimicrobial and its Evaluation of Schiff Base Transition Metal Complexes Derived from Isonicotinic Acid Hydrazide. Springer Science and Business Media LLC; 2025.
2. Kosti P, Naikoo GA, Das R, Mishra N, Kashaw S. Biological and electrochemical studies of Co^{2+}, Ni^{2+}, Cu^{2+}, Zn^{2+} and Cd^{2+} metal complexes of Schiff base ligand derived from 4-amino benzoic acid and isonicotinic hydrazide. Journal of the Iranian Chemical Society. 2021;18(7):1773-1780.
3. Uddin MN, Khandaker S, Moniruzzaman, Amin MS, Shumi W, Rahman MA, et al. Synthesis, characterization, molecular modeling, antioxidant and microbial properties of some Titanium(IV) complexes of schiff bases. J Mol Struct. 2018;1166:79-90.
4. Bulhac I, Danilescu O, Rija A, Shova S, Kravtsov VC, Bourosh PN. Cobalt(II) complexes with pentadentate Schiff bases 2,6-diacetylpyridine hydrazones: Syntheses and structures. Russian Journal of Coordination Chemistry. 2017;43(1):21-36.
5. Payehghadr M. Complexation Studies of Zn2+, Cu2+, Co2+, Ni2+ and Cd2+ Ions with a Schiff Base Ligand. Orbital - The Electronic Journal of Chemistry. 2017;9(4).
6. Almessabi A, Al-saedi K, U Ddin M, Al Naqbi M. Transformation of Operations Through Digital Twin Application. ADIPEC; 2023/10/02: SPE; 2023.
7. Ghadhyeb MZ, Abid MD. Synthesis and antimicrobial activity of silver(i) and gold(i)-bicarbene complexes with long n-alkyl chains. AIP Conference Proceedings: AIP Publishing; 2022. p. 030017.
8. Kumar M, Kumar V, Beniwal V. Synthesis of some pyrazolylaldehyde N-isonicotinoyl hydrazones and 2,5-disubstituted 1,3,4-oxadiazoles as DNA photocleaving agents. Med Chem Res. 2015;24(7):2862-2870.
9. Sedighipoor M, Kianfar AH, Kamil Mahmood WA, Azarian MH. Synthesis and electronic structure of novel Schiff bases Ni/Cu (II) complexes: Evaluation of DNA/serum protein binding by spectroscopic studies. Polyhedron. 2017;129:1-8.
10. Godoy MCM, Fighera MR, Souza FR, Flores AE, Rubin MA, Oliveira MR, et al. α2-Adrenoceptors and 5-HT receptors mediate the antinociceptive effect of new pyrazolines, but not of dipyrone. Eur J Pharmacol. 2004;496(1-3):93-97.
11. Ghadhyeb MZ, Abid AA, Abid MD. Bridge, N-heterocyclic Carbene Complexes with Silver (I) and Palladium (II): Synthesis and Biological Activity. Research Journal of Pharmacy and Technology. 2021:5366-5370.
12. Parmar N, Teraiya S, Patel R, Barad H, Jajda H, Thakkar V. Synthesis, antimicrobial and antioxidant activities of some 5-pyrazolone based Schiff bases. Journal of Saudi Chemical

Society. 2015;19(1):36-41.
13. Schau HP. V. Lorian (Editor), Antibiotics in Laboratory Medicine (Second Edition). 1259 S., 371 Abb., 323 Tab. Baltimore-London-Los Angeles-Sydney 1986. Williams and Wilkins. $ 99.00. ISBN: 0-683-05167-9. J Basic Microbiol. 1986;26(8):452-452.
14. Rosu T, Pahontu E, Maxim C, Georgescu R, Stanica N, Gulea A. Some new Cu(II) complexes containing an ON donor Schiff base: Synthesis, characterization and antibacterial activity. Polyhedron. 2011;30(1):154-162.
15. Ahamad MN, Shahid M, Ansari A, Kumar M, Khan IM, Ahmad M, et al. A combined experimental and theoretical approach to investigate the structure, magnetic properties and DNA binding affinity of a homodinuclear Cu(ii) complex. New J Chem. 2019;43(19):7511-7519.
16. Alyea EC, Malek A, Merrell PH. Synthesis and characterization of titanium (IV) Schiff base complexes, part III1. Octahedral titanium (IV) complexes of some dibasic terdentate Schiff base ligands. Transition Met Chem. 1979;4(3):172-178.
17. Lashanizadegan M, Asna Ashari H, Sarkheil M, Anafcheh M, Jahangiry S. New Cu(II), Co(II) and Ni(II) azo-Schiff base complexes: Synthesis, characterization, catalytic oxidation of alkenes and DFT study. Polyhedron. 2021;200:115148.
18. Azizah NAN, Prakoso A, Rahardjo SB, Marliyana SD. Structural characterization and antibacterial activity of aliphatic and aromatic amine of copper(II) Schiff base complexes. J Indian Chem Soc. 2025;102(12):102285.
19. J. Waheed E. Synthesis, Characterization and Biological Activity of New Ligand Derived from 4-(Dimethylamino) Benzaldehyde and Nano Copper Complex. Baghdad Science Journal. 2024.
20. Abdulah KN, Alsalihi EI, Juma JA. Synthesis, Characterization, and Biological Studies of a New Schiff Base Ligand Derived from 5-Amino-2-hydroxybenzoic Acid and Benzaldehyde and its Metal Complexes. Zanin Journal of Science and Engineering. 2025;1(3):01-20.
21. Singh N, Khan NA, Taha A, Joshi MC, Kumar P, Vedeshwar AG, et al. Synthesis, spectroscopic characterization, DFT calculations, and antimicrobial studies of novel transition metal complexes of tridentate Schiff base ligand derived from o-vanillin. J Mol Struct. 2025;1332:141722.
22. Hassan JF, Hassan SS. Preparation, Characterization, and Studying the Biological Activity of Schiff Base Metal Complexes Derived From Cephalexin With 3-Methoxy-4-Hydroxy Benzaldehyde. Baghdad Science Journal. 2025;22(10):3299-3309.
23. Suganya M, Puthilibai G. Synthesis, Spectral Characterization, Antibacterial and Anticancer Evaluation of Novel Isoniazid based Schiff Base Ligand derived Transition Metal Complexes. Asian J Chem. 2024;36(3):579-585.
24. Geraghty RJ, Capes-Davis A, Davis JM, Downward J, Freshney RI, Knezevic I, et al. Guidelines for the use of cell lines in biomedical research. Br J Cancer. 2014;111(6):1021-1046.
25. Shareef N, Wadday F. Novel Nano Schiff Base Ligand and Its Metal Complexes: Synthesis, Characterization, Molecular Docking, Antibacterial, Anticancer Evaluation Against PC-3 Cells. Al-Zahraa Journal for Health and Medical Sciences. 2026;4(1):25-50.
26. Venkatesh G, Vennila P, Kaya S, Ahmed SB, Sumathi P, Siva V, et al. Synthesis and Spectroscopic Characterization of Schiff Base Metal Complexes, Biological Activity, and Molecular Docking Studies. ACS Omega. 2024.
27. Singh G, Dalal A, Gupta S, Yadav V, Kaur J, Kaur H, et al. Design and Synthesis of Symmetric Bis Schiff Base as Potential Anti-Cancer Agent and Selective Chemosensor for Sn(II) Detection. ChemistrySelect. 2025;10(47).
28. Leoni M, Di Maggio R, Polizzi S, Scardi P. X-ray Diffraction Methodology for the Microstructural Analysis of Nanocrystalline Powders: Application to Cerium Oxide. J Am Ceram Soc. 2004;87(6):1133-1140.
29. Mirghani AH, Tahtaci H, Pehlivanoglu S, Uysal S. Synthesis and Characterization of Schiff Bases and Their Ag(I) Complexes Containing 2,5,6-Trisubstituted Imidazothiadiazole Derivatives: Molecular Docking and in Vitro Cytotoxic Effects Against Non-Small Lung Cancer Cell Line (Part 1). Elsevier BV; 2024.
30. Mohana priya T, Krishna Moorthy C, Gomathi T, M K. CNSL Based Green Catalyst Schiff Base Ligand and Its Metal(II) Complexes Synthesis, Characterization, Antibacterial, Anticancer and Molecular Docking Studies. MDPI AG; 2024.
31. Kargar H, Ashfaq M, Fallah-Mehrjardi M, Behjatmanesh-Ardakani R, Munawar KS, Tahir MN. Synthesis, crystal structure, spectral characterization, theoretical and computational studies of Ni(II), Cu(II) and Zn(II) complexes incorporating Schiff base ligand derived from 4-(diethylamino)salicylaldehyde. Inorg Chim Acta. 2022;536:120878.
32. Hamzah Daylee S, Yahya Wadday F. Synthesis and Spectroscopic Investigation of Metal Complexes with a Novel Schiff-Azo Ligand: Antibacterial Screening and Anticancer Evaluation Against MCF-7 Cells. Journal of Bioscience and Applied Research. 2025;0(0):0-0.
33. Hameed GF, Wadday FY, Salman NS. Modeling and Thermodynamic Values of Complex Equilibrium of Cobalt(II) with Diethylenetriaminepentaacetic Acid in Aqueous Solution. Indonesian Journal of Chemistry. 2021;21(3):644.
34. Yahya Wadday F, Ali Hussein A. Synthesis, Identification, Thermodynamic and Biological Studies of New Ligand Derivative from L-ascorbic acid and its Complexes with some Metal ions. Research Journal of Pharmacy and Technology. 2022:3452-3458.
35. Kumar R, Anu, Yadav V, Singh V, Pant A, Jana AK, et al. Synthesis of Fluorescent Schiff Base Hybrid Nanoparticles for Silver Extraction and their Biological Activity. ChemistrySelect. 2025;10(40).
36. Mahdi Al-Hassani Rehab A, Al-Sarray Ali J. Synthesis, Characterization, Cytotoxicity, Biological Evaluation, DFT Calculations, and Molecular Docking of a Novel Schiff Base and Its Pt(IV) Complex. Appl Organomet Chem. 2025;39(3).
37. Ayoub MA, Fahim AM, Magar HS. Novel Schiff base Cu(ii) and Au(iii) complexes: spectroscopic, computational, and electrochemical insights for H_2O_2 sensor applications. RSC Advances. 2025;15(49):41447-41470.
38. Alim MA, Bashar MA, Roy PS, Khan MN, Roy PK, Ali MS, et al. Synthesis, Physical, Spectral Characterization and Biological Studies of the complexes of Ni^{2+}, Cu^{2+}, Co^{2+} and Cd2+ions with Schiff Base Derived from p-hydroxybenzaldehyde and o-Phenyl-diamine. Oriental Journal Of Chemistry. 2024;40(5):1449-1459.
39. Paranthaman R, Moses JA, Anandharamakrishnan C. Novel powder-XRD method for detection of acrylamide in processed foods. Food Res Int. 2022;152:110893.
40. Singh K, Bala I, Kataria R, Sindhu M. Synthesis, Crystal Studies, Dft Calculations, Antimicrobial Activity and Bsa Binding Studies of Metal Complexes Derived from Pyridyl-

Based Hydrazone. Elsevier BV; 2022.
41. Akitsu T, Nakane D, Miroslaw B. Viewpoints Concerning Crystal Structure from Recent Reports on Schiff Base Compounds and Their Metal Complexes. Symmetry. 2024;16(11):1525.
42. Arabahmadi R. Cobalt (II) Complexes Derived from Azo-Azomethine Ligands: Synthesis, Characterization, Solvatochromic, Fluorescence, Thermal, Electrochemical and Antimicrobial Properties. ChemistrySelect. 2019;4(17):4883-4891.
43. Hussain SA. Synthesis, Identification and Antibacterial Study of New Ligand Derived From Benzothiazolemethanamine and its Complexes with some Metal Ions. Maaen Journal for Medical Sciences. 2025;4(1).
44. Yahya Waddai F, Kadhum Kareem E, Aqeel Hussain S. Synthesis, Spectral Characterization and Antimicrobial Activity of Some Transition Metal Complexes with new Schiff Base Ligand (BDABI). Oriental Journal of Chemistry. 2018;34(1):434-443.
45. Ejidike IP, Direm A, Parlak C, Adeniyi AA, Azam M, Ata A, et al. Spectroscopic characterization, DFT calculations, in vitro pharmacological potentials, and molecular docking studies of N, N, O-Schiff base and its trivalent metal complexes. Chemical Physics Impact. 2024;8:100549.
46. Manjula R, Pavithra C, Kumar AR, Durgadevi K, Balraj B, Selvaraj S. Exploring structural and spectroscopic aspects, solvent effect (polar and non-polar) on electronic properties, topological insights, ADME and molecular docking study of thiocolchicoside: A promising candidate for antiviral and antitumor pharmacotherapy. Spectrochimica Acta Part A: Molecular and Biomolecular Spectroscopy. 2025;331:125807.
47. Pantic D, Mirkovic N, Vulovic T, Jovanovic D, Jakovljevic S, Canovic P, et al. Evaluation of Newly Synthesized Schiff Base Pd(II) Complexes for Prostate Cancer Treatment Through In Vitro Cytotoxicity and Molecular Mechanistic Studies. MDPI AG; 2025.
48. Ghosh D, Das T, Karmakar S, Bhar S, Kar K, Mondal S, et al. A mechanistic insight into the anticancer activity of two novel metal Schiff base complexes through spectrophotometric and computational approach against melanoma. Inorg Chem Commun. 2026;184:116001.